Supplementary Information

# Decomposition of Methanol Activated by Surface Under-coordinated Pd on Layered $PdTe_2$

Jing-Wen Hsueh[1], Lai-Hsiang Kuo[1], Po-Han Chen[2], Wan-Hsin Chen[3], Chi-Yao Chuang[3], Chia-Nung Kuo[4,5], Chin-Shan Lue[4,5,6], Hung-Wei Shiu[7], Bo-Hong Liu[7], Chia-Hsin Wang[7], Yao-Jane Hsu[7], Chun-Liang Lin,[3,8*] Jyh-Pin Chou[9,*] and Meng-Fan Luo[1,*]

[1]Department of Physics, National Central University, No. 300 Jhongda Rd., Jhongli District, Taoyuan 320317, Taiwan

[2]Department of Materials Science and Engineering, National Tsing Hua University, 101, Section 2 Kuang Fu Road, Hsinchu 300044, Taiwan

[3]Department of Electrophysics, National Yang Ming Chiao Tung University, No. 1001 University Rd., Hsinchu 300039, Taiwan

[4]Department of Physics, National Cheng Kung University, No. 1 University Rd., Tainan 70101, Taiwan

[5]Taiwan Consortium of Emergent Crystalline Materials, National Science and Technology Council, Taipei 10601, Taiwan

[6]Program on Key Materials, Academy of Innovative Semiconductor and Sustainable Manufacturing, National Cheng Kung University, Tainan 70101, Taiwan

[7]National Synchrotron Radiation Research Center, No.101 Hsin-Ann Rd., Hsinchu Science Park, Hsinchu 300092, Taiwan

[8]Center for Emergent Functional Matter Science, National Yang Ming Chiao Tung University, No. 1001 University Rd., Hsinchu 300039, Taiwan

[9]Graduate School of Advanced Technology, National Taiwan University, No. 1, Sec. 4, Roosevelt Rd., Taipei 106319, Taiwan

**Corresponding authors:** Meng-Fan Luo (mfl28@phy.ncu.edu.tw); Jyh-Pin Chou (jpchou@cc.ncue.edu.tw); Chun-Liang Lin (clin@nycu.edu.tw)

Figure S1 shows a wide-range PES spectrum from the as-cleaved $PdTe_2$. Such a wide-range PES survey was performed before each set of experiments to confirm negligible contamination (primarily carbon species). As shown in the figure, the signals associated with carbon species, near 284 -287 eV, are negligible.

Figure S2 compares the STM image (Figure S2a) to the DFT-simulated one (Figure S2b) produced based on a single $Te_{top}$ vacancy model (Figure 1e). The well match of these two images corroborates that the dark spots (areas) indeed correspond to the $Te_{top}$ vacancies.

Figures S3a,b exemplify the surface morphology of $PdTe_2$ bombarded with $Ar^+$ for longer time (a greater $Ar^+$ dosage). In addition to the formation of $Te_{top}$ vacancies, the roughness was obviously increased. The lateral profile (Figure S3b) shows that both the islands‘ heights and cavities’ depths exceed evidently the depth of $Te_{top}$ vacancies (~ 0.12 nm). These islands could be $PdTe_2$ patches and Pd-Te nanoclusters formed by nucleation of re-deposited Pd and Te. Therefore, structurally different $Pd_{uc}$-X, such as those at the edges of $PdTe_2$ patches and re-deposited Pd-Te nanoclusters, were generated with such a greater $Ar^+$ dosage. To reduce the structural complexity, a controlled $Ar^+$ dosage was employed to prepare our samples for the investigation of catalytic properties. Figures S3c,d compare the RHEED patterns obtained from at the [100] azimuth of $PdTe_2$ before and after $Ar^+$ bombardment. The sharp and bright reflection rods from as-cleaved $PdTe_2$ (Figure S3c) suggest a highly crystalline $PdTe_2$ surface; the patterns correspond to a hexagonal lattice with a lattice constant of 4.11 Å, quite close to the value obtained from STM (Figure 1). The reflection rods became faint

(Figure S3d) after $Ar^+$ bombardment, suggesting attenuated surface crystallinity — the extent of ordered $PdTe_2$ structures decreased. Besides, no additional diffraction patterns were formed so the re-deposited Pd-Te nanoclusters had no long-range structural ordering.

Figure S4 shows Pd 3d and Te 4d PES spectra from layered $PdTe_2$ as cleaved and bombarded by $Ar^+$ (0.5 keV) for (a,b) 120 and (c,d) 30 s. The Pd 3d lines broadened after the $Ar^+$ bombardment (lower panel), because an additional feature grew at a BE slightly smaller than that of the main Pd feature, 341.6 eV for Pd $3d_{3/2}$ and 336.3 eV for Pd $3d_{5/2}$, indicated by red fitted curves. The smaller BE for Pd 3d implies less oxidized Pd, such as $Pd_{uc}$, at the $PdTe_2$ surface and therefore the removal of Te atoms by the $Ar^+$ bombardment. In contrast, the Te 4d doublet altered little in its line shape after $Ar^+$ bombardment. These spectral features for varied $Ar^+$ dosages are similar despite varied intensities of the $Pd_{uc}$ features. The $Pd_{uc}$ signals thus correspond not only to the $Pd_{uc}$ at the $Te_{top}$ vacancies ($Pd_{uc}$-V) but possibly to those at other surface defects ($Pd_{uc}$-X) generated by greater $Ar^+$ dosages (Figure S3).

Figure S5a shows the C 1s signals were absent for the $Ar^+$-bombarded $PdTe_2$ exposed to CO at 145 K. The result indicates that CO did not adsorb on defective $PdTe_2$ surface at 145 K. Therefore, the carbon species (from decomposed methanol) which yielded C 1s signals about 285.2 eV, is assigned to $CH_xO$* species, instead of CO*. Figure S3b shows the C* yielded signals centered at 284.3 eV; accordingly, the carbon species which yielded C 1s signals about 283.6 eV, is not C* but $CH_x$*.

Figure S6 shows the DFT modelling for adsorption of methanol and its decomposition intermediates or fragments on structurally perfect $PdTe_2$ surface and the $Te_{top}$ divacancy. Varied

adsorption configurations and corresponding adsorption energies are also given. The results indicate that the adsorption energies on the $Te_{top}$ divacancy are in general stronger than those on pristine $PdTe_2$ surface; either methanol or its decomposition intermediates (or fragments) is preferentially bonded to $Pd_{uc}$-V at the $Te_{top}$ divacancy.

Figures S7 –S17 shows the computed energetic barriers of three main decomposition processes, including dehydrogenation from either oxygen or carbon, and C-O bond scission (deoxygenation and dehydroxylation), at varied stages on the $Te_{top}$-divacancy site. There are no barriers for the inverse processes CHOH* + H* $\rightarrow$ $CH_2OH$* (Figure S13) and $CH_2O$* + H* $\rightarrow$ $CH_2OH$* (Figure S14). The result suggests that the dehydrogenation of $CH_2OH$* to either CHOH* or $CH_2O$* would not occur; instead, $CH_2O$* can readily combine with H* to yield $CH_2OH$*. As $CH_2O$* also readily combines with H* to yield $CH_3O$* (Figure 6b), no stable $CH_2O$* exists on the surface. We thus observed no desorption of $CH_2O_{(g)}$. Figures S15-S17 shows the barriers for dehydrogenation of $CH_x$* to $CH_{x-1}$* (x = 1-3). It is noted these barriers are evidently greater than those of hydrogenation, the inverse processes. Accordingly, $CH_4$*, instead of C*, is preferentially formed. Figure S18 shows a small barrier for the hydrogenation of $CH_3$* to $CH_4$*. The $CH_{4(g)}$ is thus heavily produced whereas C* is little.

Figure S19 shows the calculated barriers of a hydroxyl group (OH*) diffusing from the $Pd_{uc}$-V sites to the basal plane and between $Te_{top}$ sites on the basal plane (Figure S19). These barriers 0.95 and 0.27 eV are smaller than those for the reactions (Figure 6b), so with the progress of methanol decomposition, the produced OH* diffuses easily away from the active sites or combines with H* to

desorb as $H_2O_{(g)}$ (Figure 5c). The obstruction of the active $Pd_{uc}$-V sites by either C* and OH* during the reaction is ignorable.

Figure S20 compares projected density of states (PDOS) of $Pd_{uc0-3}$-V at $PdTe_2$ surface and Pd at Pd(111) surface; $Pd_{uc0}$-V stands for the Pd in structurally perfect $PdTe_2$, $Pd_{uc1-3}$-V stands for Pd with 1-3 missing Te-Pd bonds (coordination number 5-3) at $PdTe_2$ surface. Figures S21-S25 show the simulated dehydrogenation of $CH_3OH$* to $CH_2O$* and $CH_2OH$*, and dehydroxylation of $CH_2OH$* to $CH_2$* in the $Te_{top}$-trivacancy model. The simulation suggests the reaction should proceed in a manner similar to that on a $Te_{top}$-divacancy model. Enlarging the $Te_{top}$ vacancies (increasing the number of $Pd_{uc3}$-V) is expected to yield similar results, instead of altering the reaction pathway.

As the coordination (to Te) number of $Pd_{uc}$-V determines its electronic structure and as larger $Te_{top}$ vacancies are also generated in the present study, we introduce a $Te_{top}$-trivacancy model with a $Pd_{uc3}$-V at the center to confirm the effect of the coordination number of $Pd_{uc}$-V on the catalytic performance. The adsorption energies of the main intermediates and the reaction barriers of several key processes in the divacancy and trivacancy models are shown to be comparable (Figure. S21**)**. For instance, the computed barriers for dehydrogenation of $CH_3OH$* to $CH_3O$* and then to $CH_2O$* amount to 1.65 and 1.17 eV (Figures S22 and S23), respectively; the dehydrogenation of $CH_3OH$* to $CH_2OH$* does not occur (Figure S24) and the dehydroxylation of $CH_2OH$* to $CH_2$* and OH* has a barrier about 1.81 eV (Figure S25). The comparison suggests that $Pd_{uc3}$-V and $Pd_{uc2}$-V as single-atom catalysts toward methanol decomposition play similar roles; enlarging the $Te_{top}$ vacancies (increasing the

number of $Pd_{uc3}$-V) is expected to yield similar results, instead of altering the reaction pathway. The different catalytic properties observed at $Pd_{uc}$ concentrations > 20 % (Figure 4) result from structurally different $Pd_{uc}$-X.

Figure S26 schematically illustrates the structure of the edges of a $PdTe_2$ island and also shows the activation energies for dehydrogenation and dehydroxylation of methanol ($CH_3OH$) on the edge sites of a $PdTe_2$ island. The $Pd_{uc}$ at the edges consist primarily of $Pd_{uc1}$-X atoms; details about this edge-site model can be found in Ref. 1. The detailed information on the energy barrier calculations is provided in Figures S27 - S28. Also, the adsorption energies of related species are calculated and indicated in the parentheses. In the light of a much smaller barrier for desorption (0.66 eV), the methanol would prefer desorption to decomposition. The result implies that increasing the edge $Pd_{uc1}$-X sites decreases the average conversion probability (to both $CH_xO$* and $CH_x$*) on $Pd_{uc}$ sites.

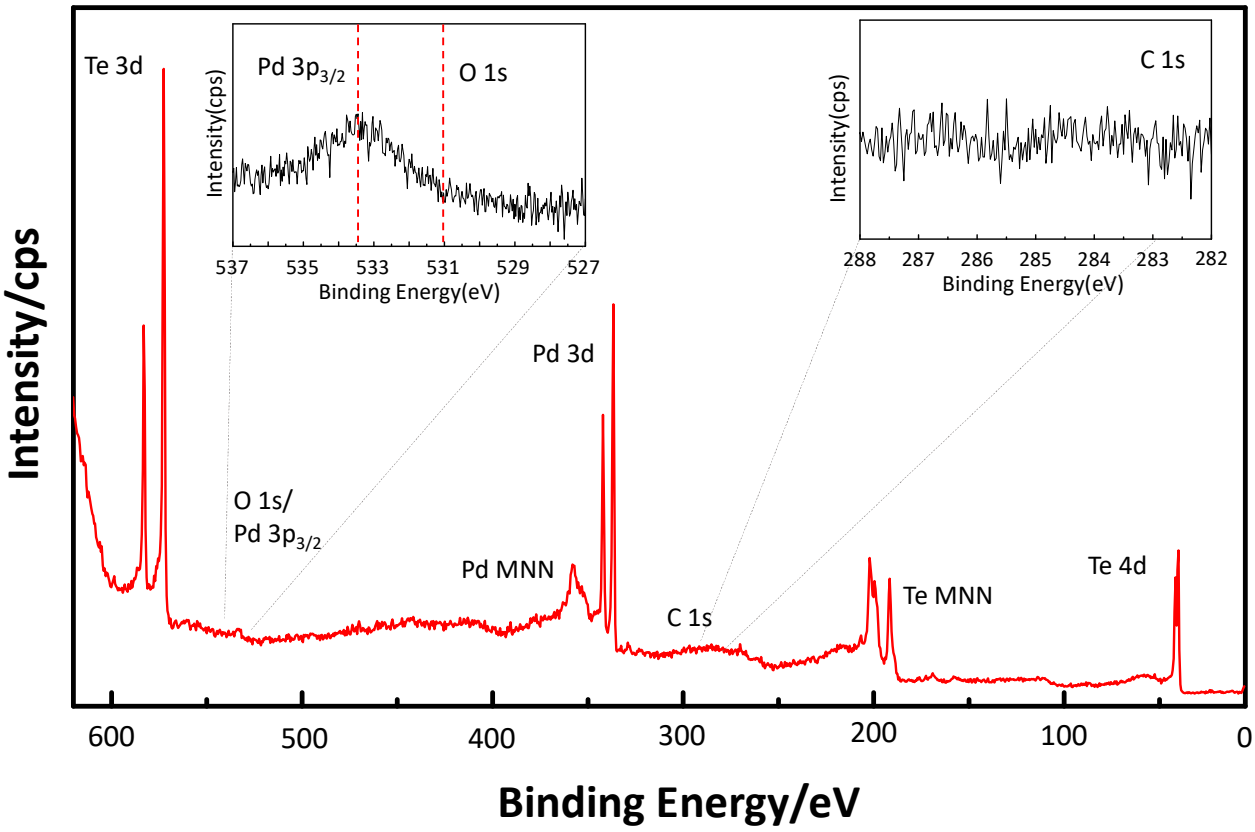


**Figure S1** a wide-range PES spectrum from the as-cleaved $PdTe_2$. A photon energy 680 eV was used for the measurement.

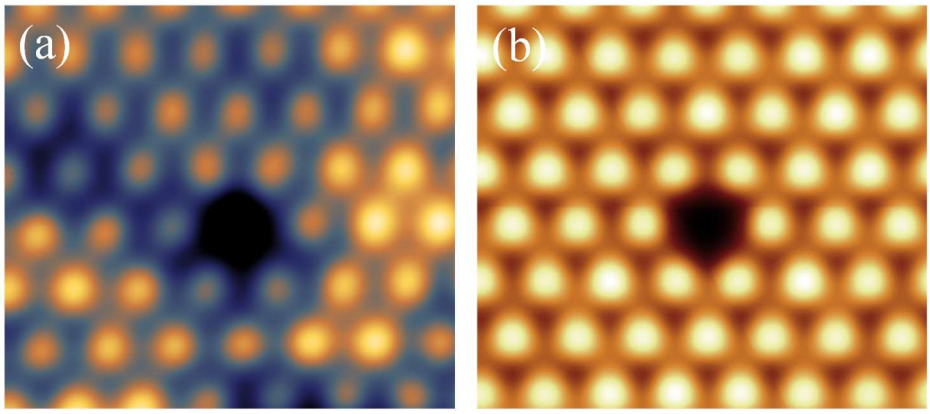


**Figure S2.** Comparison of (a) the STM image ($V_s$ = -1.0 V, $I_t$ = 0.3 nA) with (b) the DFT-simulated one produced based on a single $Te_{top}$ vacancy model (as shown Figure 1e). In (b), yellow balls denote the simulated images for the $Te_{top}$ atoms; the simulated image was derived with a bias of −1.0 V.

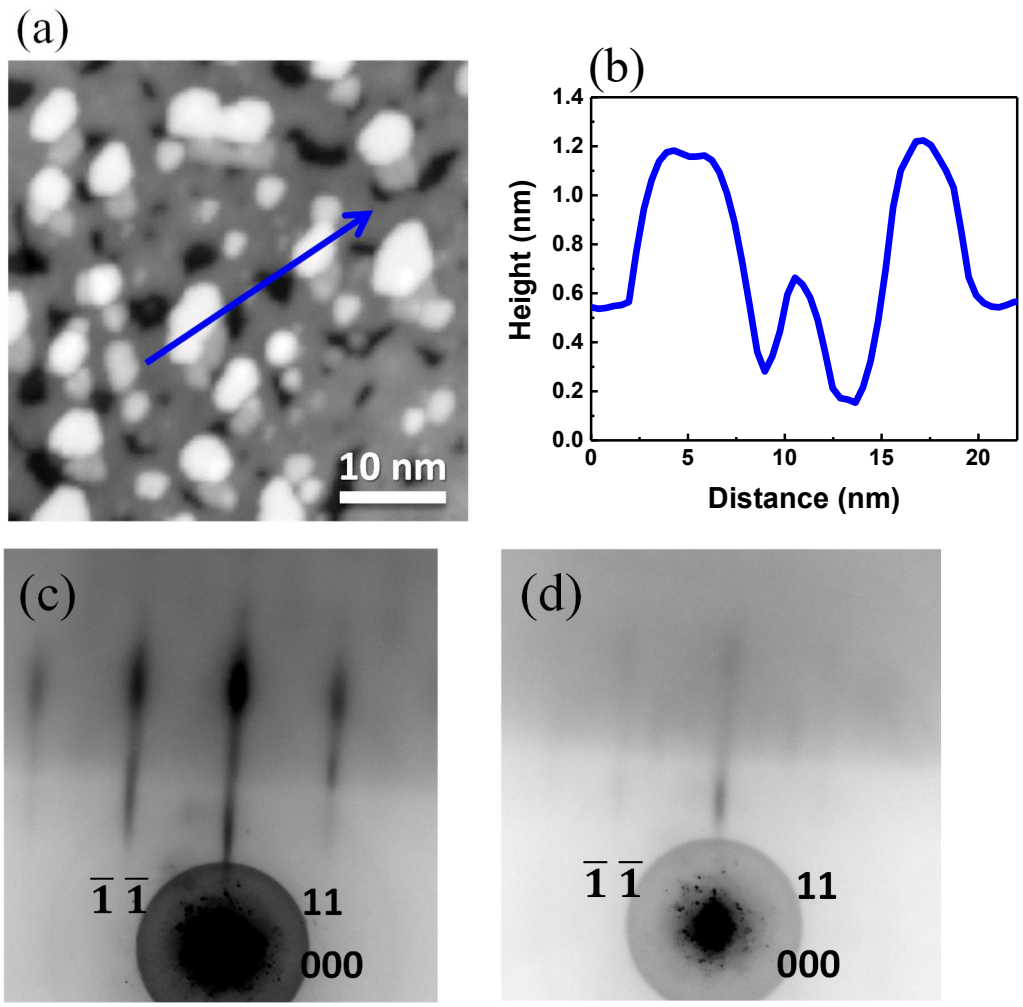


**Figure S3.** (a) STM image ($V_s$ = −810 mV, $I_t$ = 0.5 nA) of $PdTe_2$ surface bombarded by $Ar^+$ (0.5 keV, 0.7 μA · 180 s); (b) a depth profile along the blue arrow in (a). Comparison of RHEED patterns obtained from $PdTe_2$ (c) before and (d) after $Ar^+$ bombardment (0.5 keV, 0.7 μA · 180 s). The RHEED measurements were performed with an incident electron beam of 25 keV at a grazing angle of 2° to 3° relative to the surface, and the patterns were obtained at the [100] azimuth of $PdTe_2$ substrate.

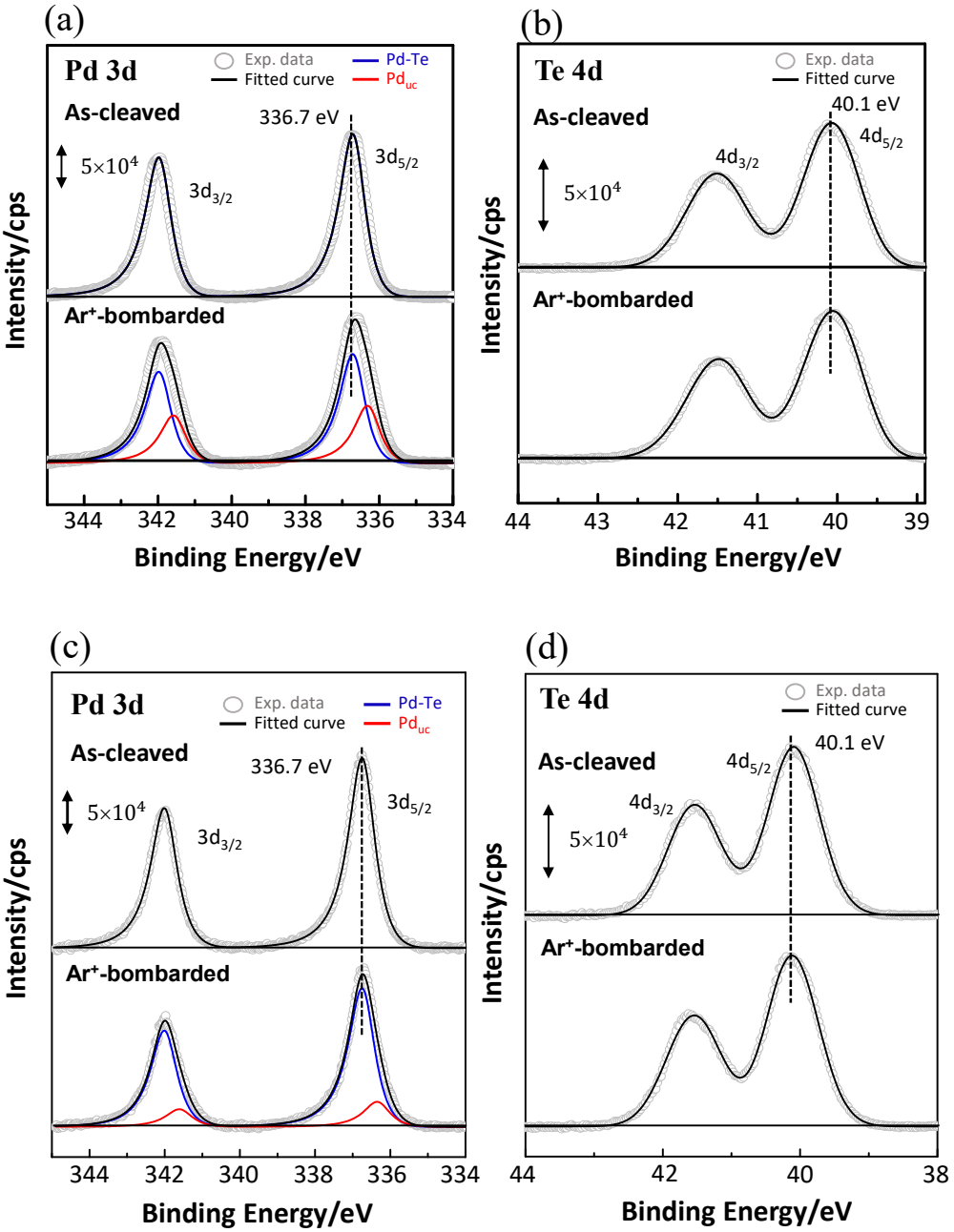


**Figure S4** PES spectra of Pd 3d and Te 4d core levels from layered $PdTe_2$ as cleaved and bombarded by $Ar^+$ (0.5 keV) for (a,b) 120 and (c,d) 30 s; In (a) - (d), gray circles and black lines denote the spectra and the sum of fitted curves, respectively; the signals from intact Pd and $Pd_{uc}$ in the layered $PdTe_2$ are fitted with blue and red lines, respectively.

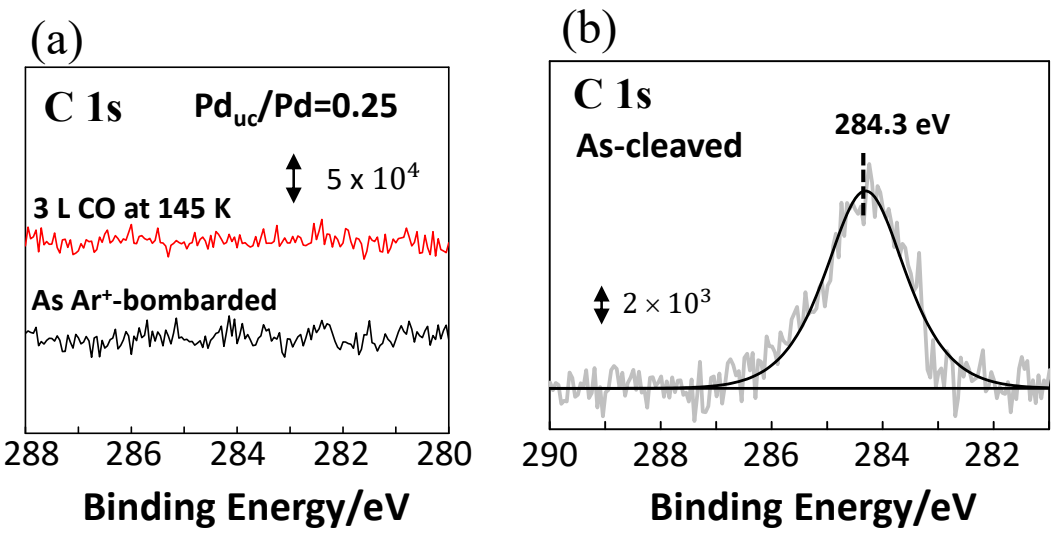


**Figure S5.** PES spectra of C 1s core level for (a) $Ar^+$-bombarded $PdTe_2$ exposed to 3.0 L CO at 145 K (red line) and (b) as-cleaved $PdTe_2$ surface contaminated by atomic carbon (C*). In (a), the C 1s spectrum for $Ar^+$-bombarded $PdTe_2$ without exposure to CO was also presented (bottom, black line) as a comparison. In (c), the black curve is the fitted one for the C* signals.

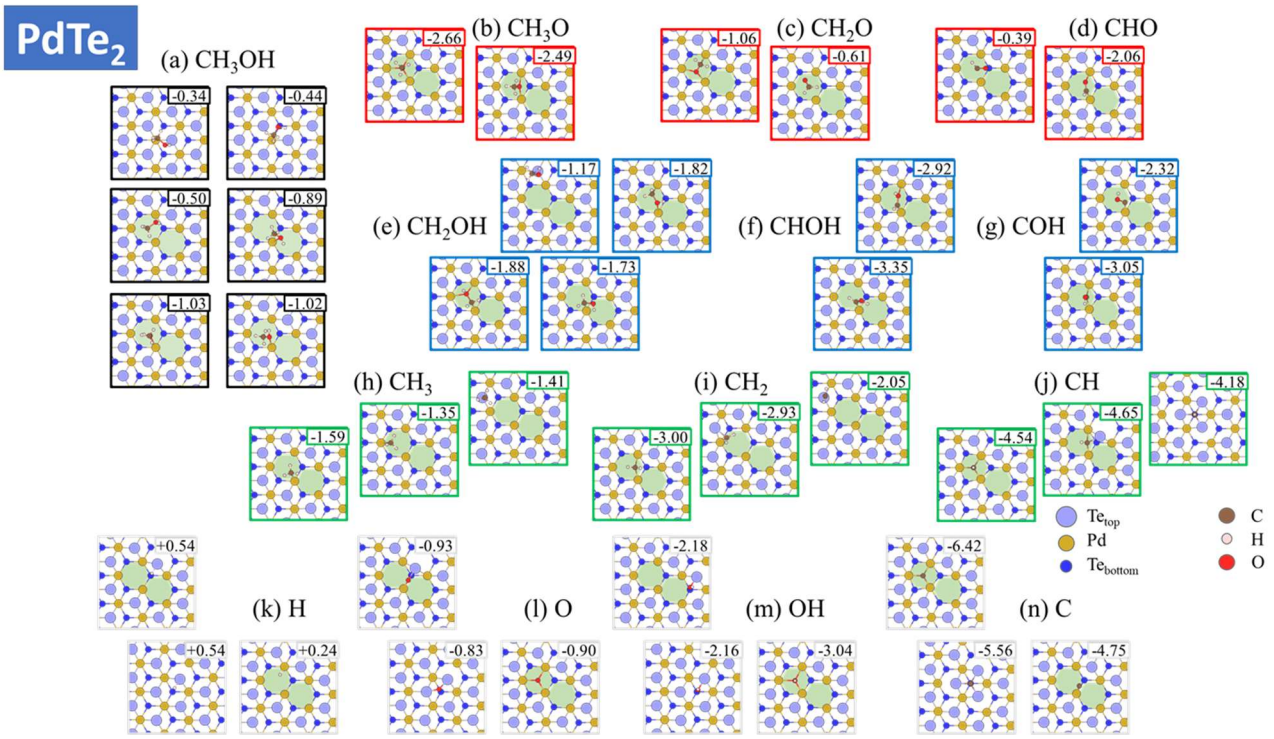


**Figure S6.** Varied adsorption configurations of methanol and its decomposition intermediates or fragments in the $Te_{top}$ divacancy model. For the sake of clarity, the $Te_{top}$-divacancy site is shadowed with green. The value at the top-right corner of each graph is provided for the corresponding adsorption energy.

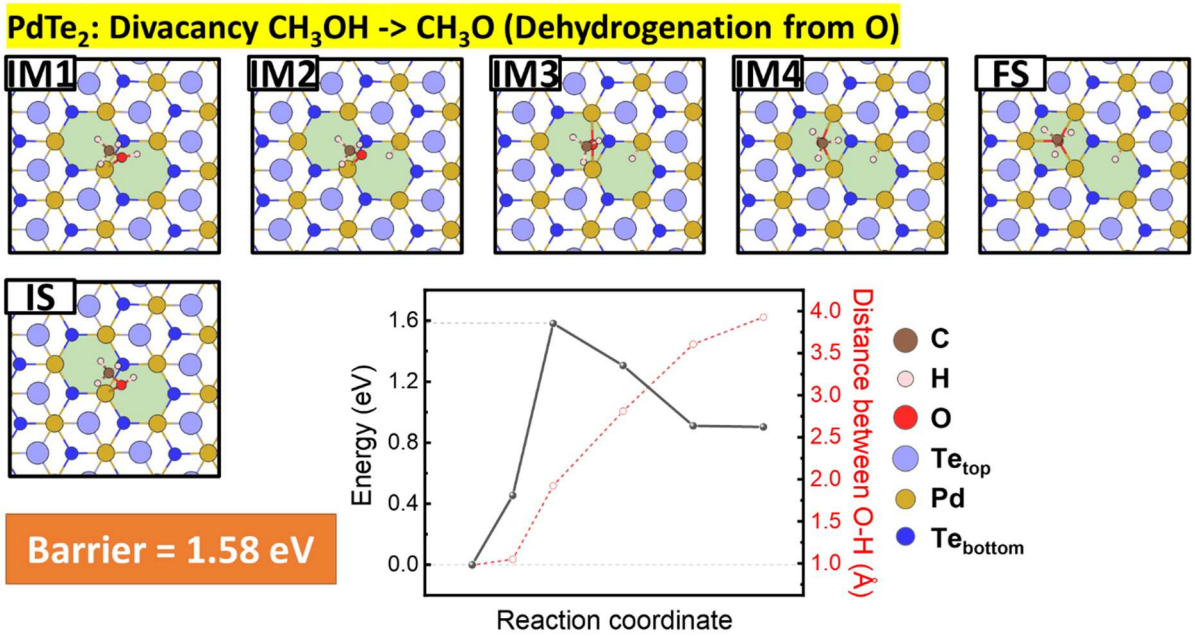


**Figure S7.** The energy profile of dehydrogenation of methanol ($CH_3OH$) to methoxy ($CH_3O$) on the $Te_{top}$-divacancy site (shadowed with green). The energy barrier is 1.58 eV. Details of initial state (IS), CINEB images (IM) and final state (FS) are presented. The red dashed line indicates the variation of the O-H distance.

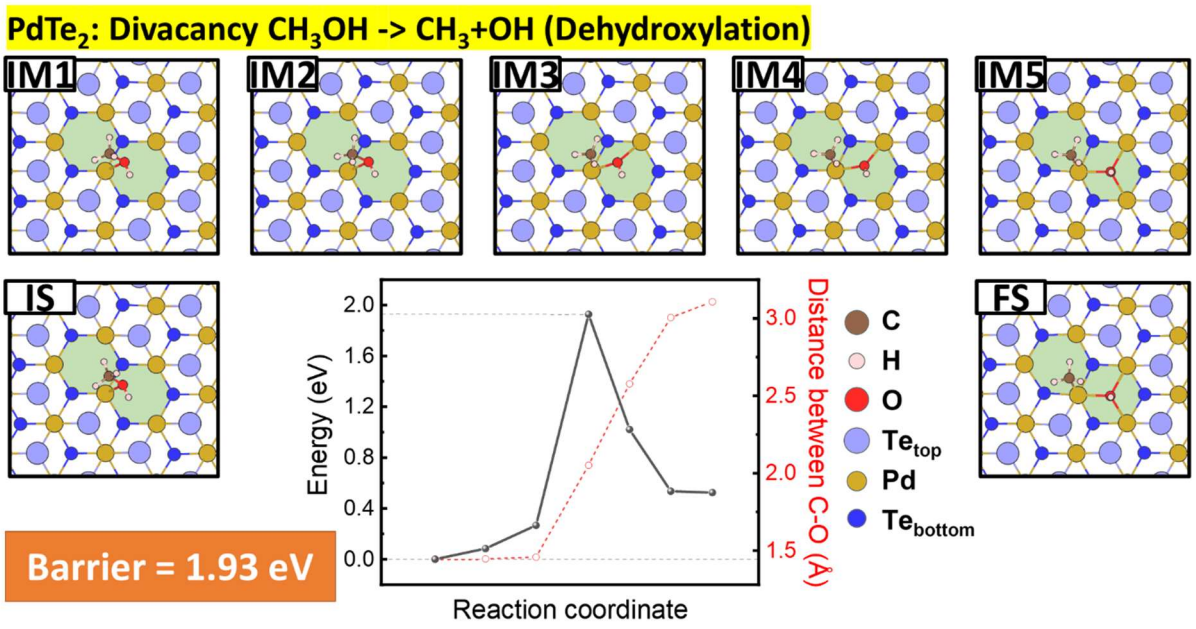


**Figure S8.** The energy profile of methanol ($CH_3OH$) C-O bond scission on the $Te_{top}$-divacancy site (shadowed with green). The energy barrier is 1.93 eV. Details of initial state (IS), CINEB images (IM) and final state (FS) are presented. The red dashed line indicates the variation of the C-O distance.

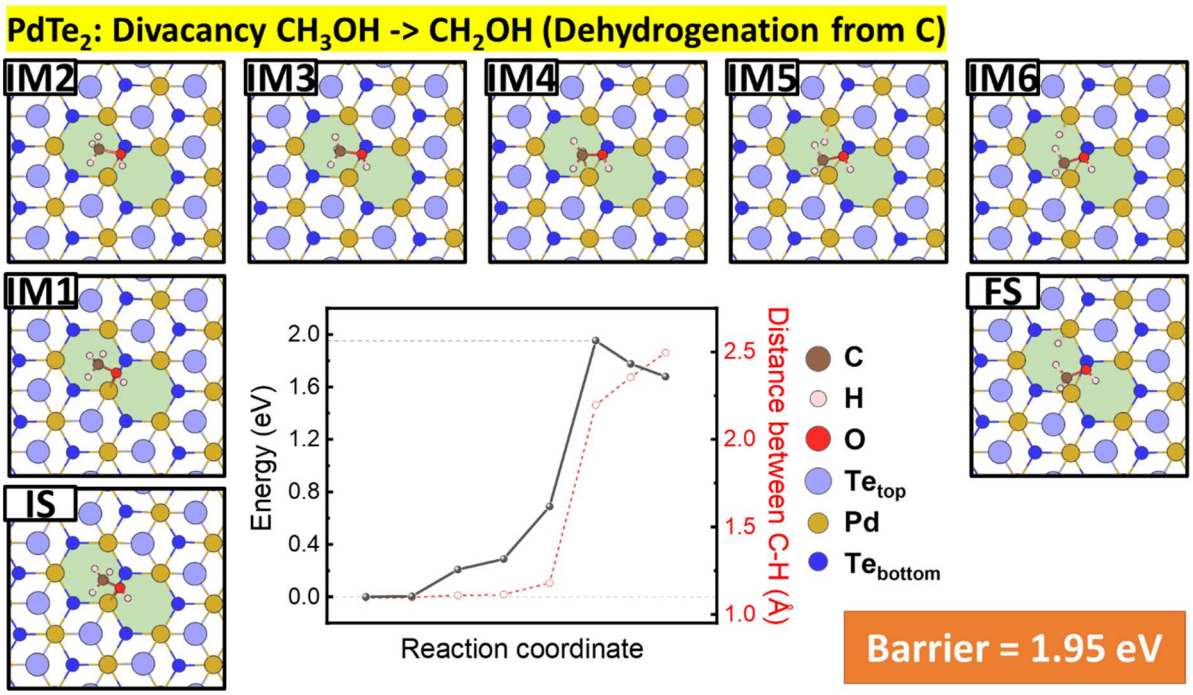


**Figure S9.** The energy profile of dehydrogenation of methanol ($CH_3OH$) to hydroxymethyl ($CH_2OH$) on the $Te_{top}$-divacancy site (shadowed with green). The energy barrier is 1.95 eV. Details of initial state (IS), CINEB images (IM) and final state (FS) are presented. The red dashed line indicates the variation of the C-H distance.

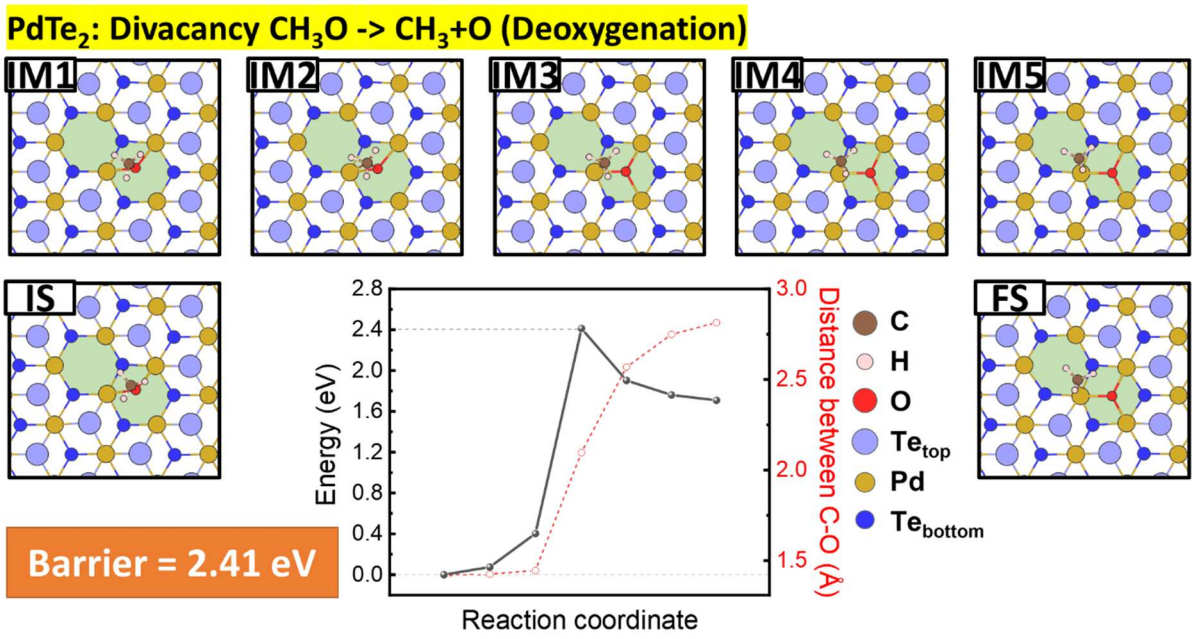


**Figure S10.** The energy profile of methoxy ($CH_3O$) C-O bond scission on the $Te_{top}$-divacancy site (shadowed with green). The energy barrier is 2.41 eV. Details of initial state (IS), CINEB images (IM) and final state (FS) are presented. The red dashed line indicates the variation of the C-O distance.

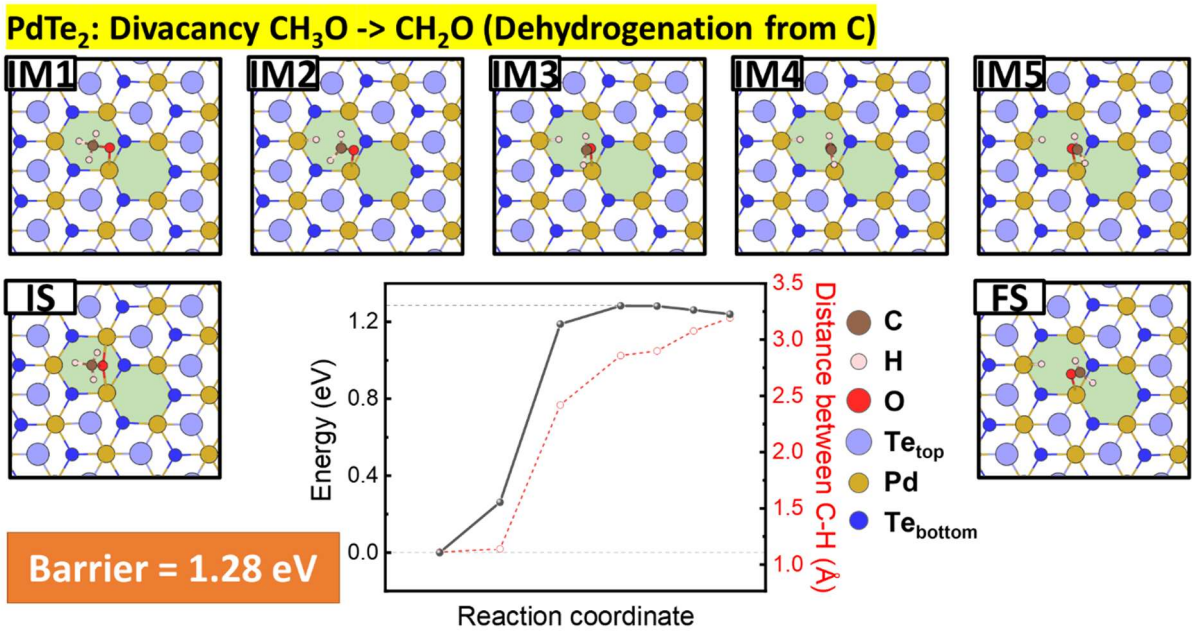


**Figure S11.** The energy profile of dehydrogenation of methoxy ($CH_3O$) to formaldehyde ($CH_2O$) on the $Te_{top}$-divacancy site (shadowed with green). The energy barrier is 1.28 eV. Details of initial state (IS), CINEB images (IM) and final state (FS) are presented. The red dashed line indicates the variation of the C-H distance.

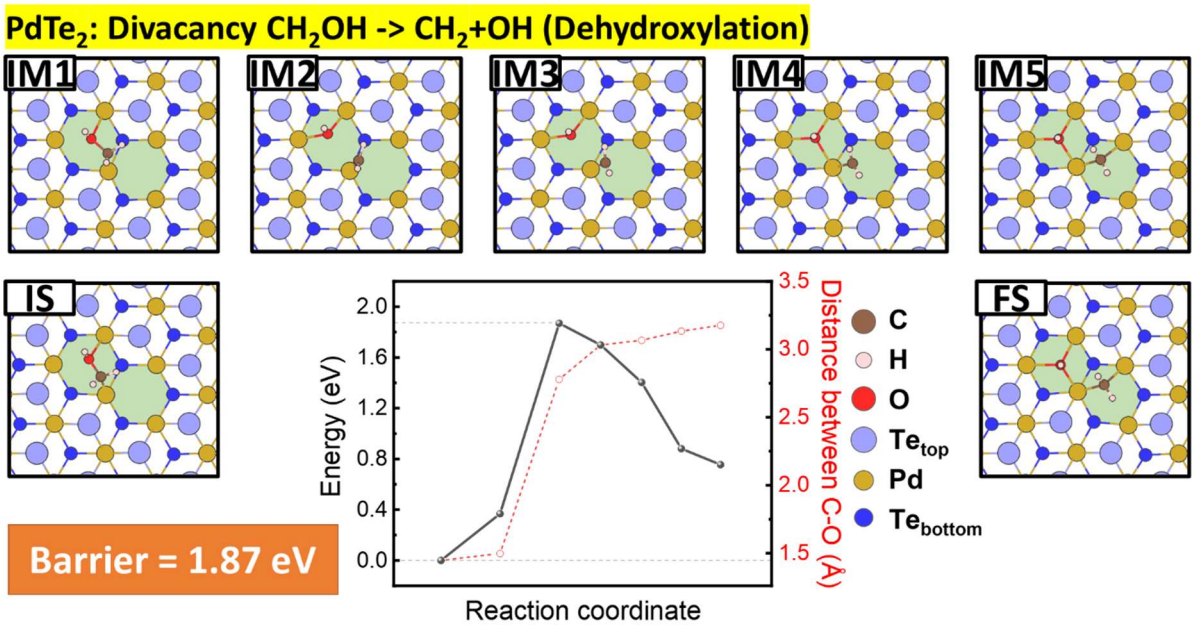


**Figure S12.** The energy profile of hydroxymethyl ($CH_2OH$) C-O bond scission on the $Te_{top}$-divacancy site (shadowed with green). The energy barrier is 1.87 eV. Details of initial state (IS), CINEB images (IM) and final state (FS) are presented. The red dashed line indicates the variation of the C-O distance.

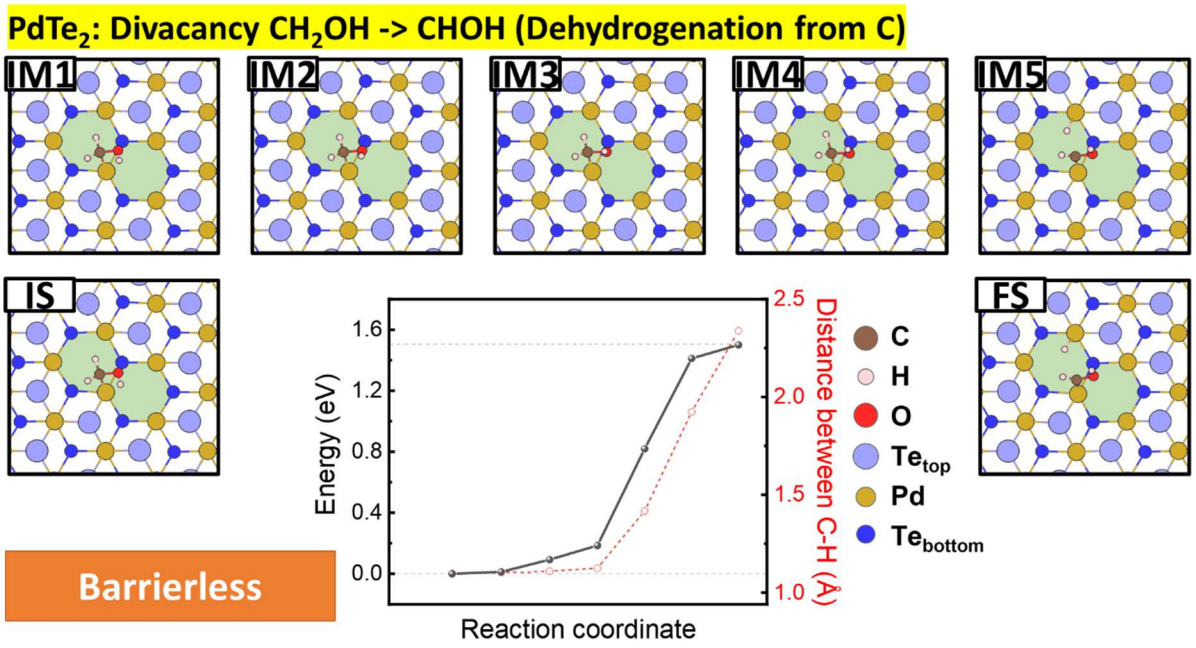


**Figure S13.** The energy profile of dehydrogenation of hydroxymethyl ($CH_2OH$) to CHOH on the $Te_{top}$-divacancy site (shadowed with green). The energy barrier is 1.46 eV but the inverse process (CHOH* + H* $\rightarrow$ $CH_2OH$*) has a negligible barrier and $CH_2OH$* has a lower total energy. Therefore, the process will not occur. Details of initial state (IS), CINEB images (IM) and final state (FS) are presented. The red dashed line indicates the variation of the C-H distance.

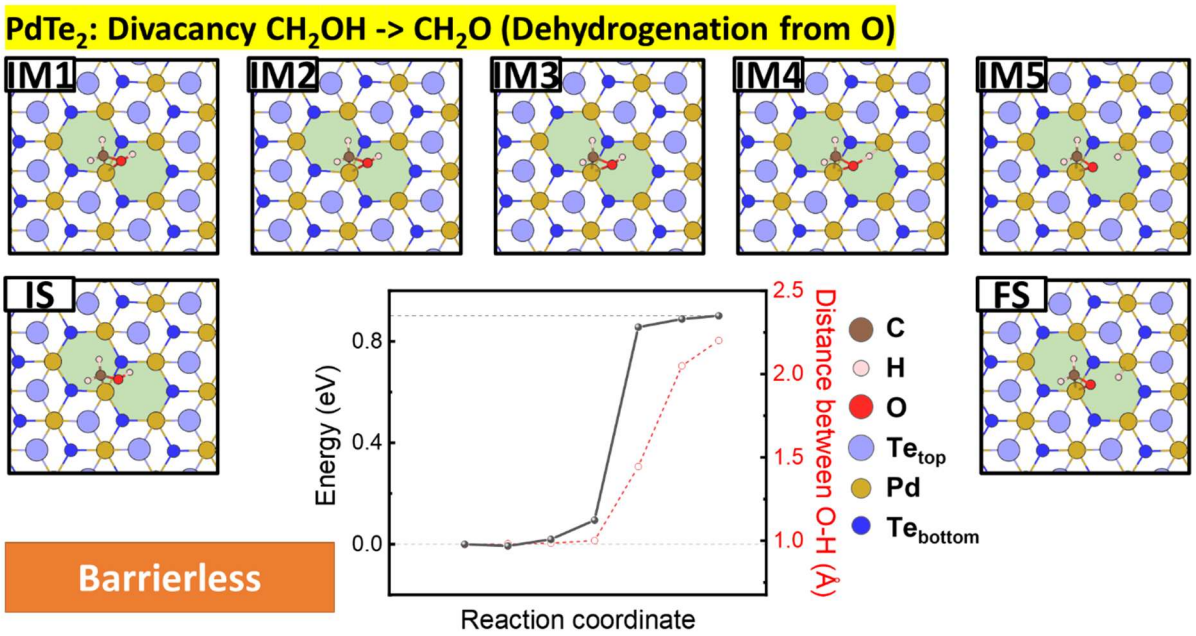


**Figure S14.** The energy profile of dehydrogenation of hydroxymethyl ($CH_2OH$) to formaldehyde ($CH_2O$) on the $Te_{top}$-divacancy site (shadowed with green). The energy barrier is 0.90 eV but the inverse process ($CH_2O^* + H^* \rightarrow CH_2OH^*$) has a negligible barrier and $CH_2OH^*$ has a lower total energy. Therefore, the process will not occur. Details of initial state (IS), CINEB images (IM) and final state (FS) are presented. The red dashed line indicates the variation of the O-H distance.

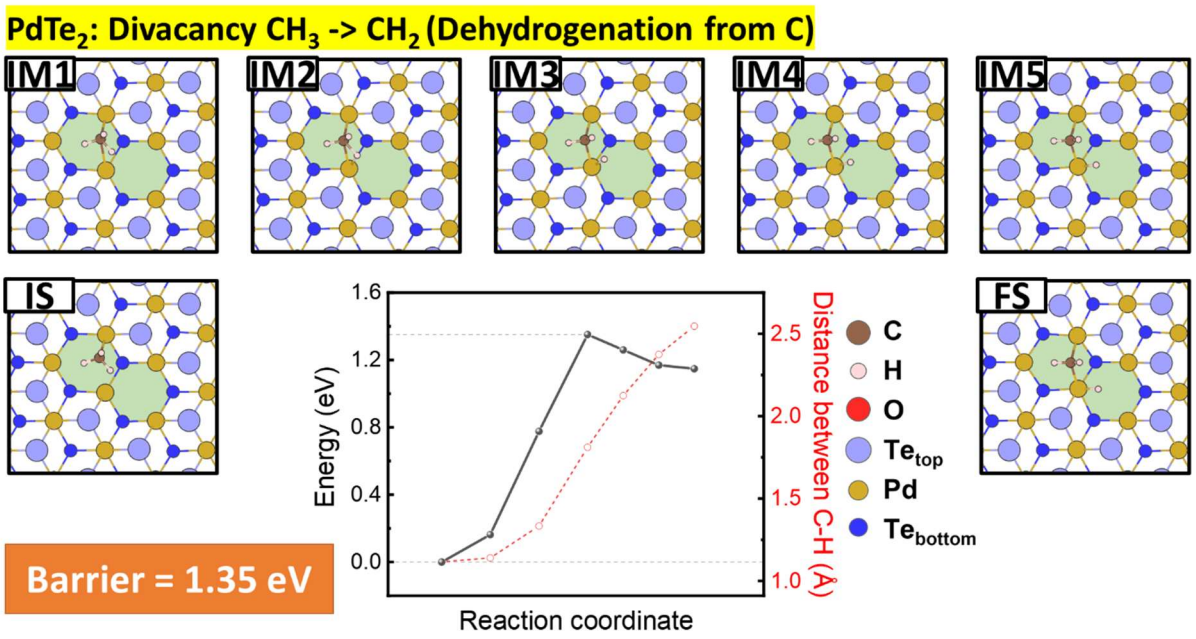


**Figure S15.** The energy profile of dehydrogenation of $CH_3$* to $CH_2$* on the $Te_{top}$-divacancy site (shadowed with green). The energy barrier is 1.35 eV but the inverse process ($CH_2$* + H* → $CH_3$*) has a barrier 0.20 eV and $CH_3$* has a lower total energy. Details of initial state (IS), CINEB images (IM) and final state (FS) are presented. The red dashed line indicates the variation of the C-H distance.

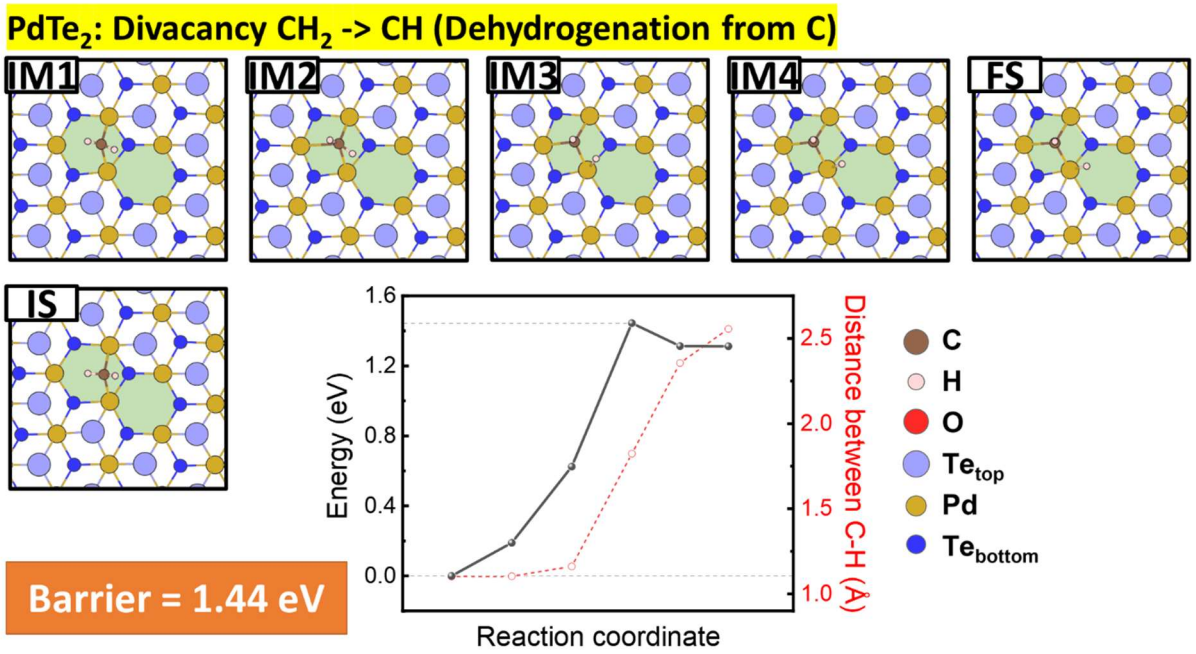


**Figure S16.** The energy profile of dehydrogenation of $CH_2$* to CH* on the $Te_{top}$-divacancy site (shadowed with green). The energy barrier is 1.44 eV but the inverse process ($CH_1$* + H* → $CH_2$*) has a barrier 0.13 eV and $CH_3$* has a lower total energy. Details of initial state (IS), CINEB images (IM) and final state (FS) are presented. The red dashed line indicates the variation of the C-H distance.

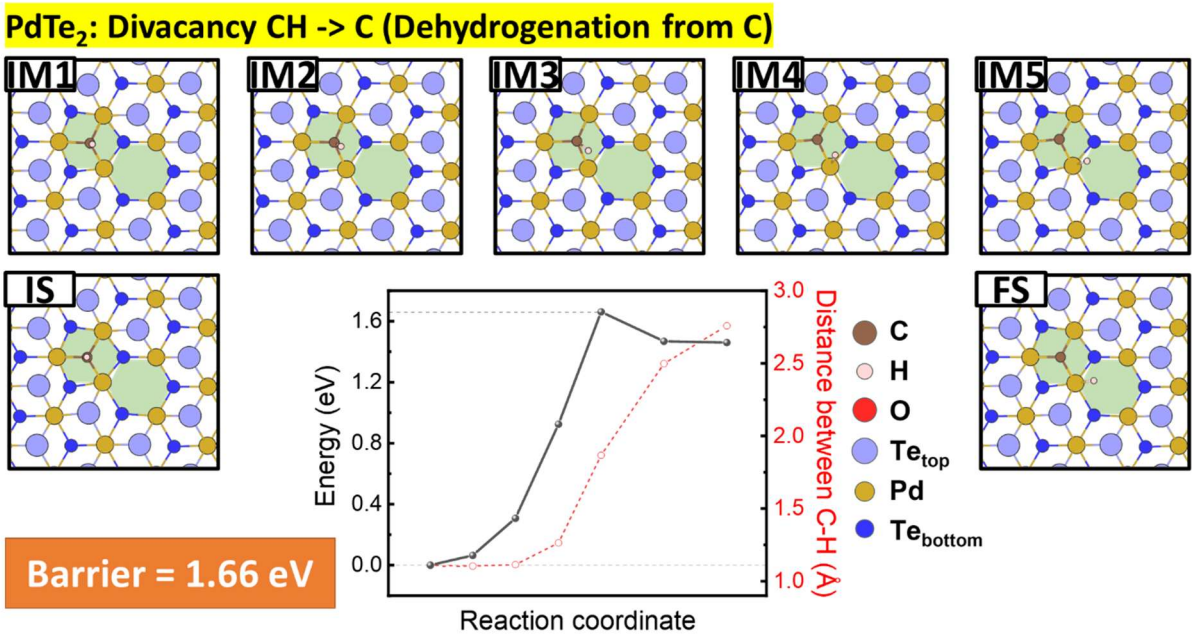


**Figure S17.** The energy profile of dehydrogenation of CH* to C* on the $Te_{top}$-divacancy site (shadowed with green). The energy barrier is 1.66 eV but the inverse process (C* + H* → $CH_1$*) has a barrier 0.20 eV and CH* has a lower total energy. Details of initial state (IS), CINEB images (IM) and final state (FS) are presented. The red dashed line indicates the variation of the C-H distance.

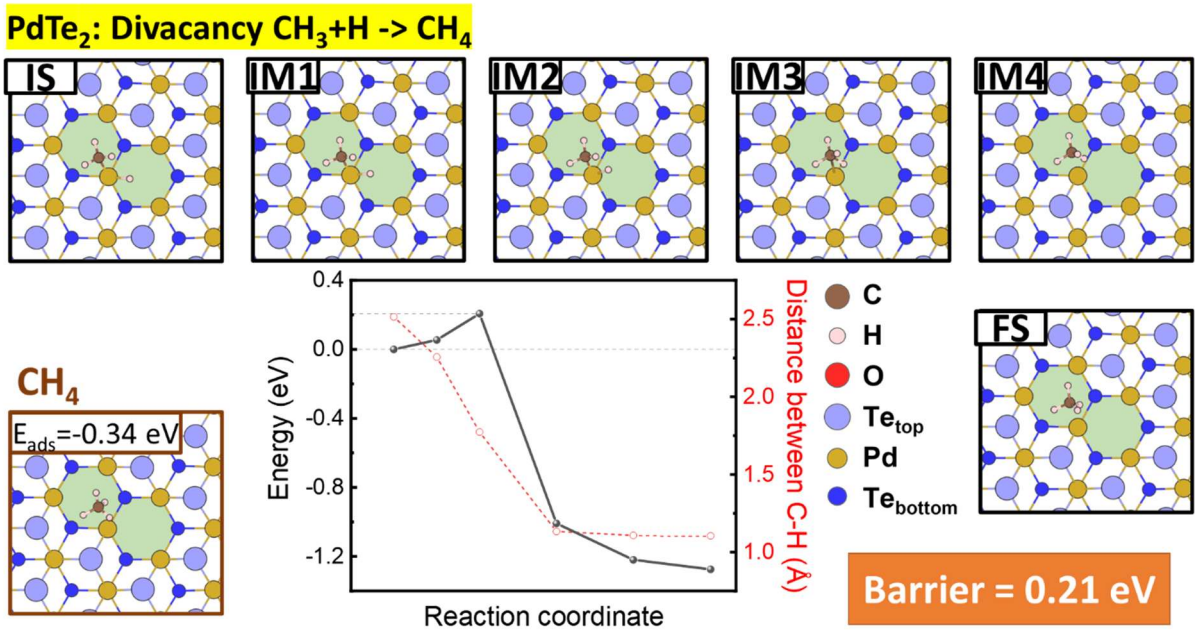


**Figure S18.** The energy profile of hydrogenation of $CH_3$* to $CH_4$* on the $Te_{top}$-divacancy site (shadowed with green). The energy barrier is 0.21 eV and $CH_4$* has a lower total energy. Details of initial state (IS), CINEB images (IM) and final state (FS) are presented. The red dashed line indicates the variation of the C-H distance.

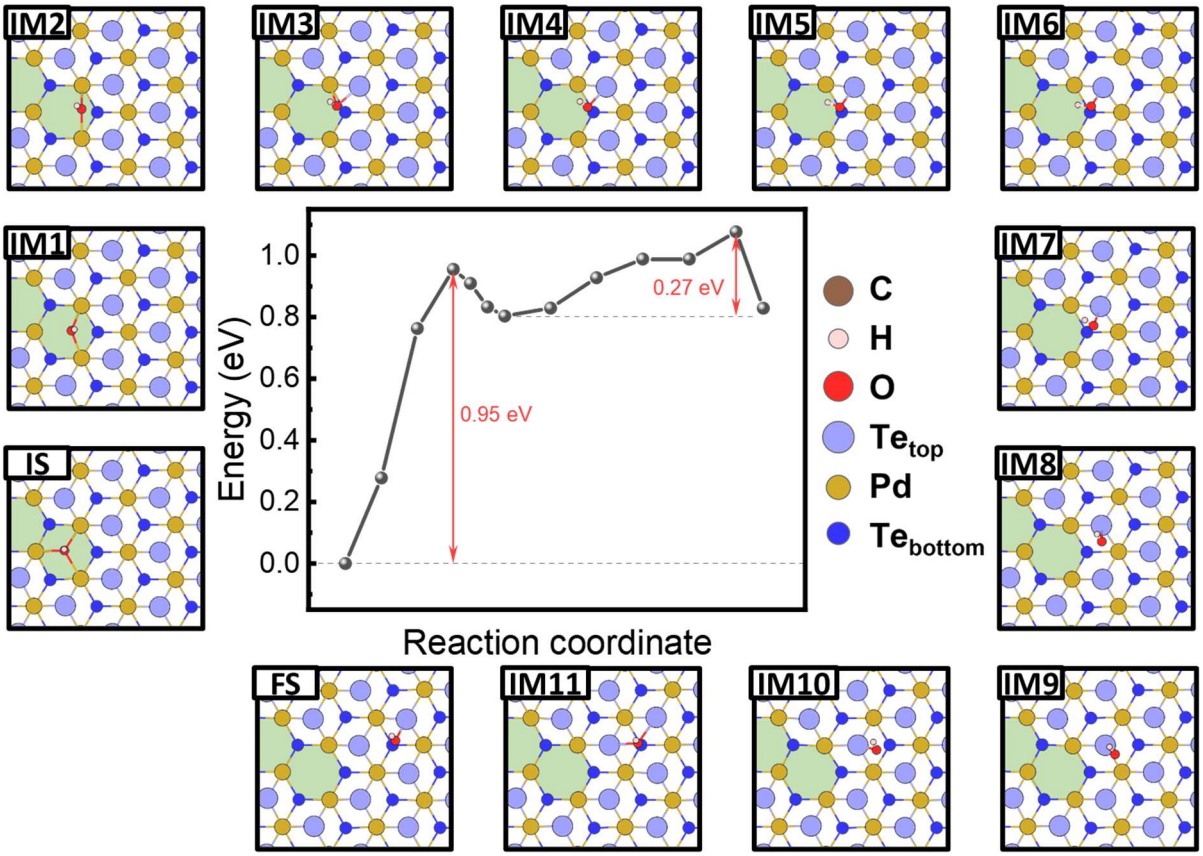


**Figure S19.** The energy profile of hydroxyl (OH*) diffusion from the divacancy defect site to the $PdTe_2$ basal plane. The energy barriers are indicated (red) in the figure. Details of initial state (IS), CINEB images (IM), and final state (FS) are presented.

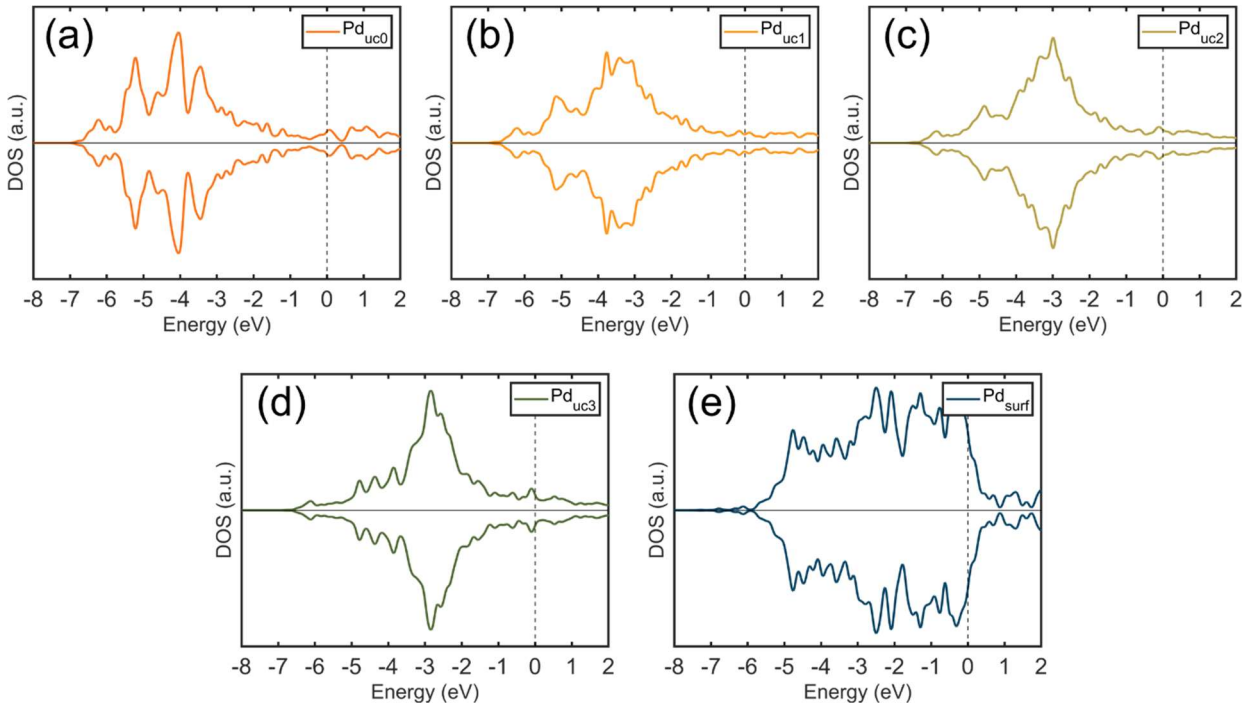


**Figure S20.** Comparison of projected density of states (PDOS) of (a)-(d) $Pd_{uc0\text{-}3}$-V at $PdTe_2$ surface and (e) Pd at Pd(111) surface. $Pd_{uc0}$-V stands for the Pd in structurally perfect $PdTe_2$, $Pd_{uc1\text{-}3}$-V stands for Pd with 1-3 missing Te-Pd bonds (coordination number 5-3) at $PdTe_2$ surface. The result in (e) was obtained from a Pd(111) surface model — a (1×1) supercell with 7 Pd layers.

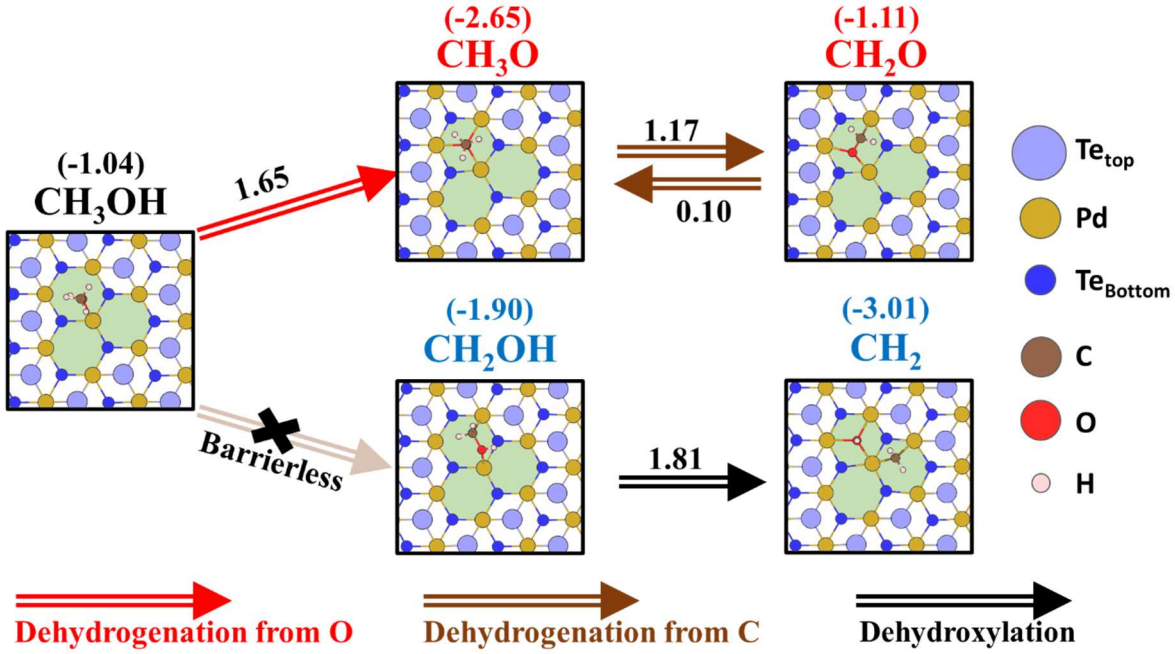


**Figure S21.** Dehydrogenation of $CH_3OH$* to $CH_2O$* and $CH_2OH$*, and dehydroxylation of $CH_2OH$* to $CH_2$* in the $Te_{top}$-trivacancy model. The adsorbed methanol first dehydrogenates to methoxy ($CH_3O$) and then to formaldehyde ($CH_2O$), with energy barriers of 1.65 and 1.17 eV, respectively, but cannot dehydrogenate to $CH_2OH$* because the inverse process, the inverse process ($CH_2OH$* + H* → $CH_3OH$*) has no barrier. The dehydroxylation of $CH_2OH$* to $CH_2$* on the other hand has a barrier about 1.81 eV. The detailed information on the energy barrier calculations is provided in Figures S20-S23. Also, the adsorption energies of related species are calculated and indicated in the parentheses, with the adsorption configurations shown in the panels.

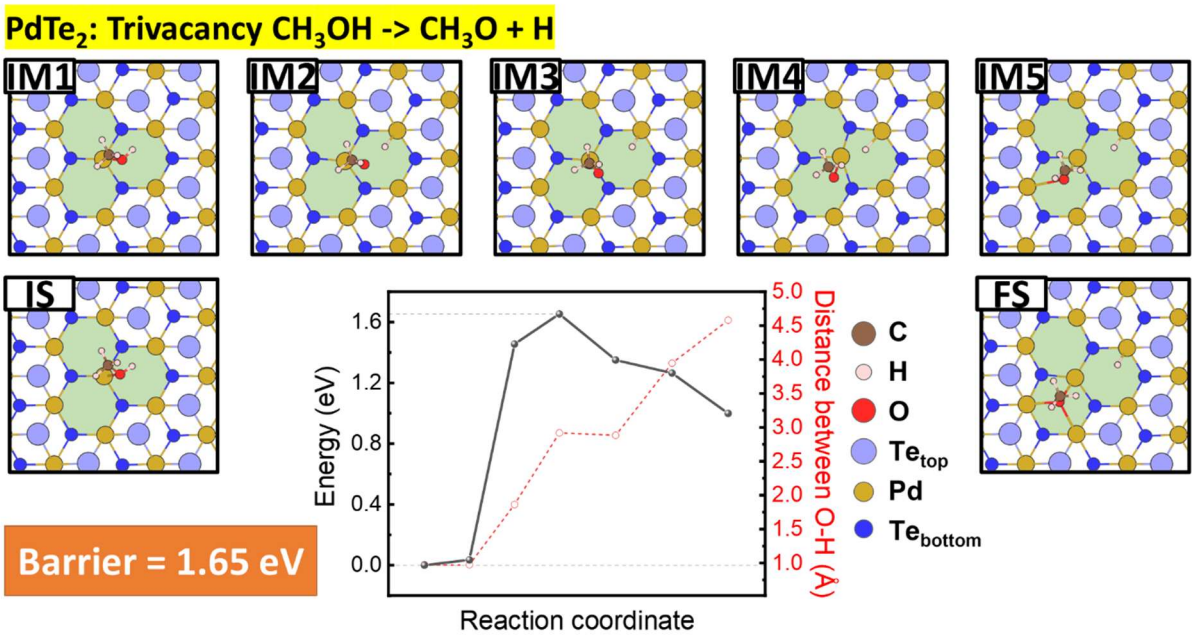


**Figure S22.** The energy profile of dehydrogenation of $CH_3OH^*$ to $CH_3O^*$ on the $Te_{top}$-trivacancy site (shadowed with green). The energy barrier is near 1.65 eV. Details of initial state (IS), CINEB images (IM) and final state (FS) are presented. The red dashed line indicates the variation of the O-H distance.

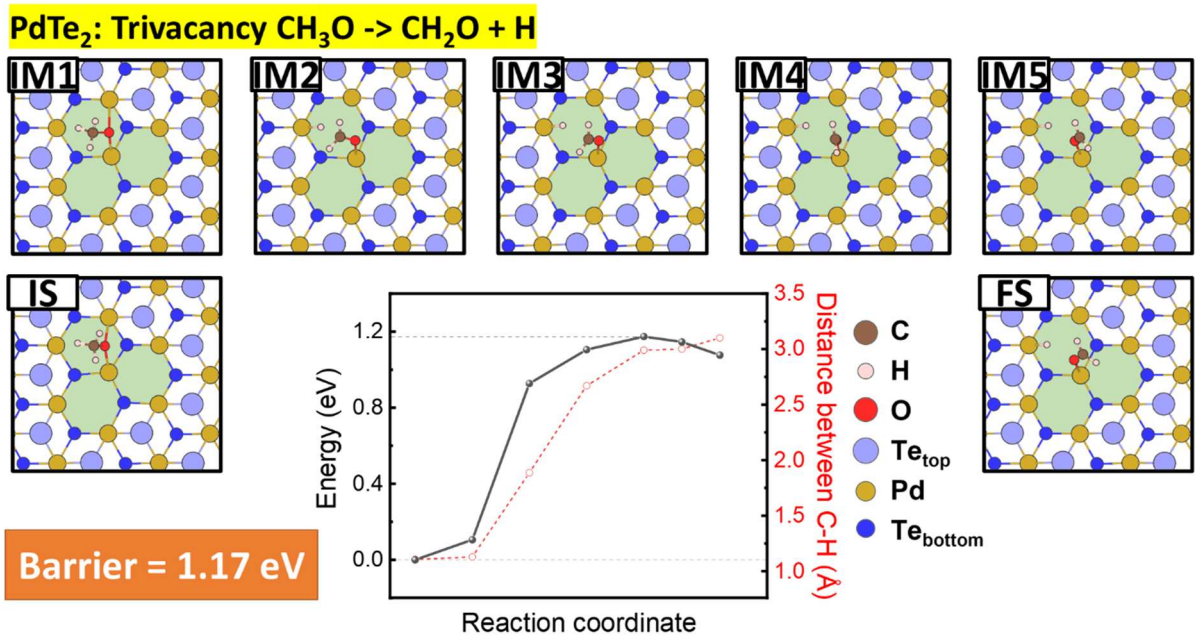


**Figure S23.** The energy profile of dehydrogenation of $CH_3O$* to $CH_2O$* on the $Te_{top}$-trivacancy site (shadowed with green). The energy barrier is near 1.17 eV. Details of initial state (IS), CINEB images (IM) and final state (FS) are presented. The red dashed line indicates the variation of the C-H distance.

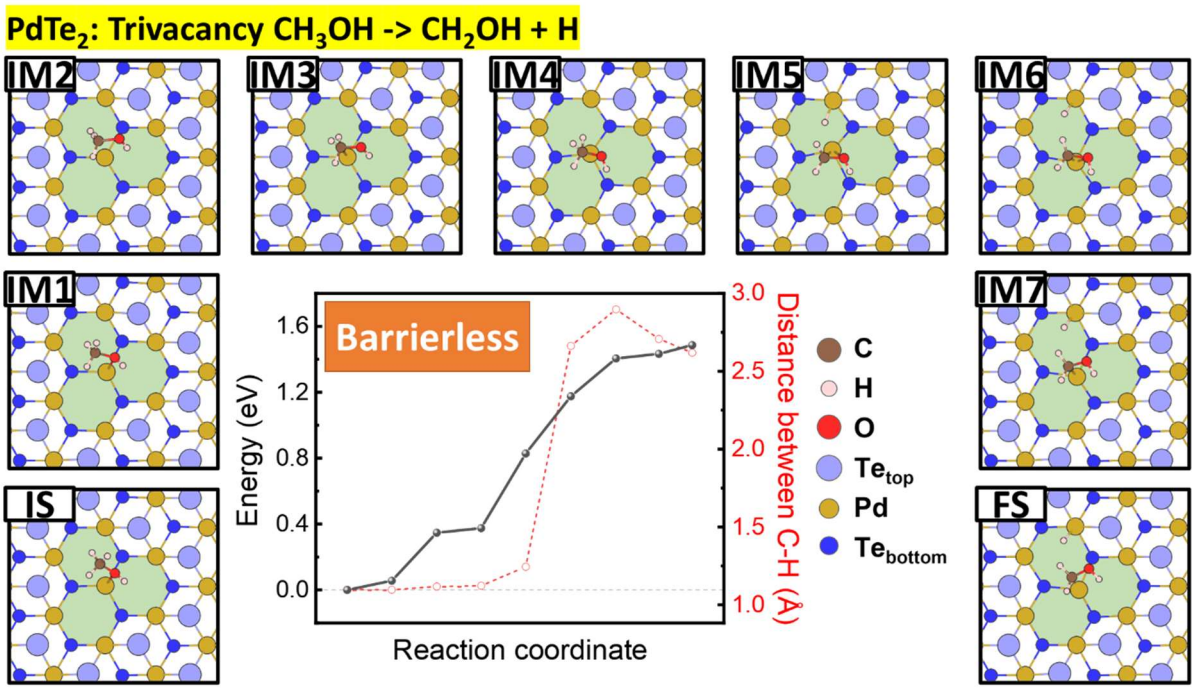


**Figure S24.** The energy profile of dehydrogenation of $CH_3OH^*$ to $CH_2OH^*$ on the $Te_{top}$-trivacancy site (shadowed with green). The energy barrier is near 1.55 eV but the inverse process ($CH_2OH^* + H^* \rightarrow CH_3OH^*$) has no barrier and $CH_3OH^*$ has a lower total energy. Therefore, the process will not occur. Details of initial state (IS), CINEB images (IM) and final state (FS) are presented. The red dashed line indicates the variation of the C-H distance.

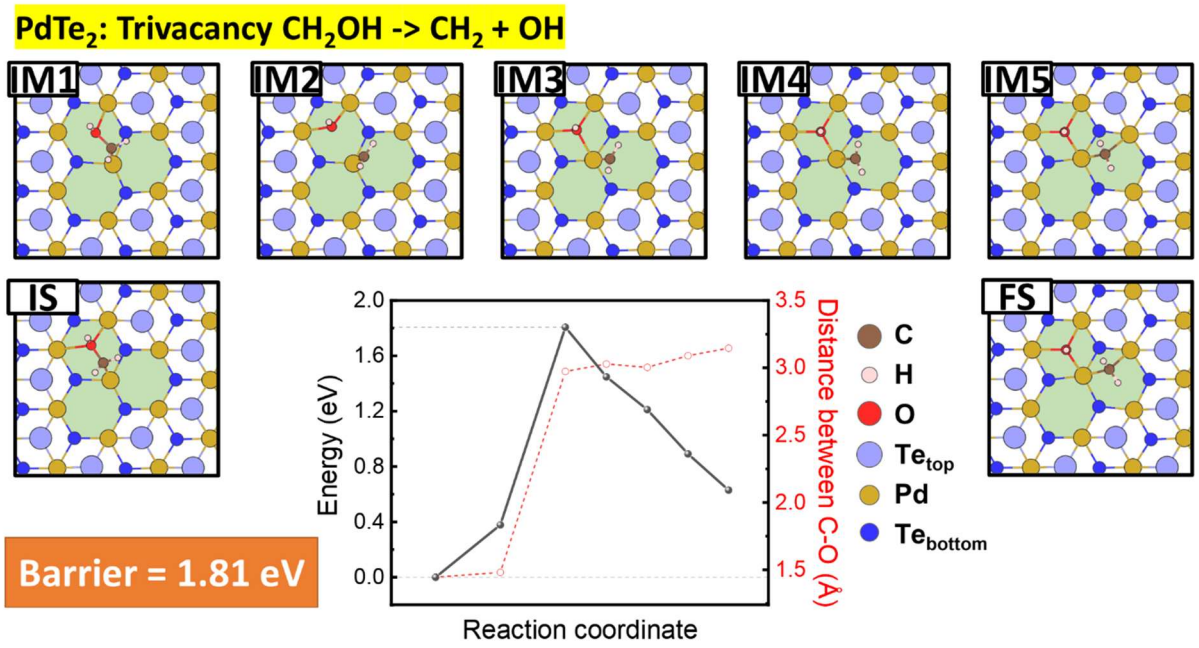


**Figure S25.** The energy profile of dehydroxylation of $CH_2OH$* to $CH_2$* and OH* on the $Te_{top}$-trivacancy site (shadowed with green). The energy barrier is 1.81 eV, comparable to that (1.87 eV) on the $Te_{top}$-divacancy site (Figure S10). Details of initial state (IS), CINEB images (IM) and final state (FS) are presented. The red dashed line indicates the variation of the C-O distance.

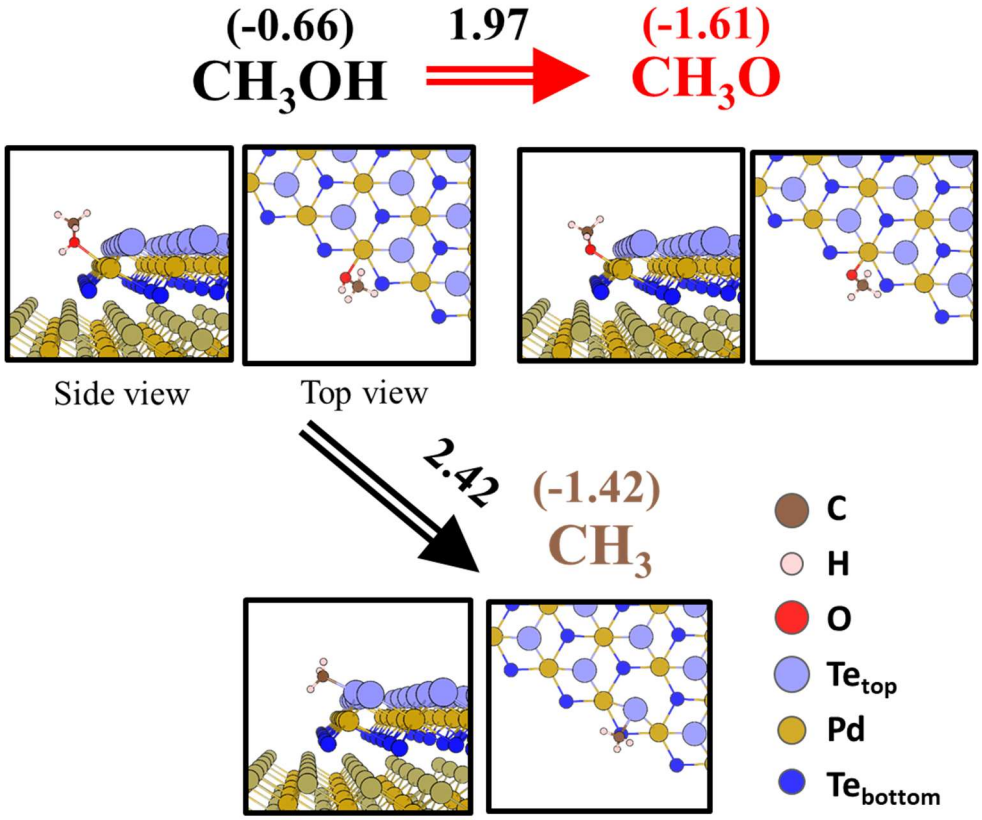


**Figure S26.** Dehydrogenation and dehydroxylation of methanol ($CH_3OH$) on the edge sites of a $PdTe_2$ island. The adsorbed methanol dehydrogenates to methoxy ($CH_3O$) by overcoming an energy barrier of 1.97 eV. Alternatively, the methanol decomposes via C-O bond scission to yield $CH_3$ and OH, with an energy barrier of 2.42 eV. The detailed information on the energy barrier calculations is provided in Figures S25 - S26. Also, the adsorption energies of related species are calculated and indicated in the parentheses, with the adsorption configurations shown in the panels. In the light of a much smaller barrier for desorption (0.66 eV), the methanol would prefer desorption to decomposition. Details about this edge-site model can be found in Ref. 1.

.

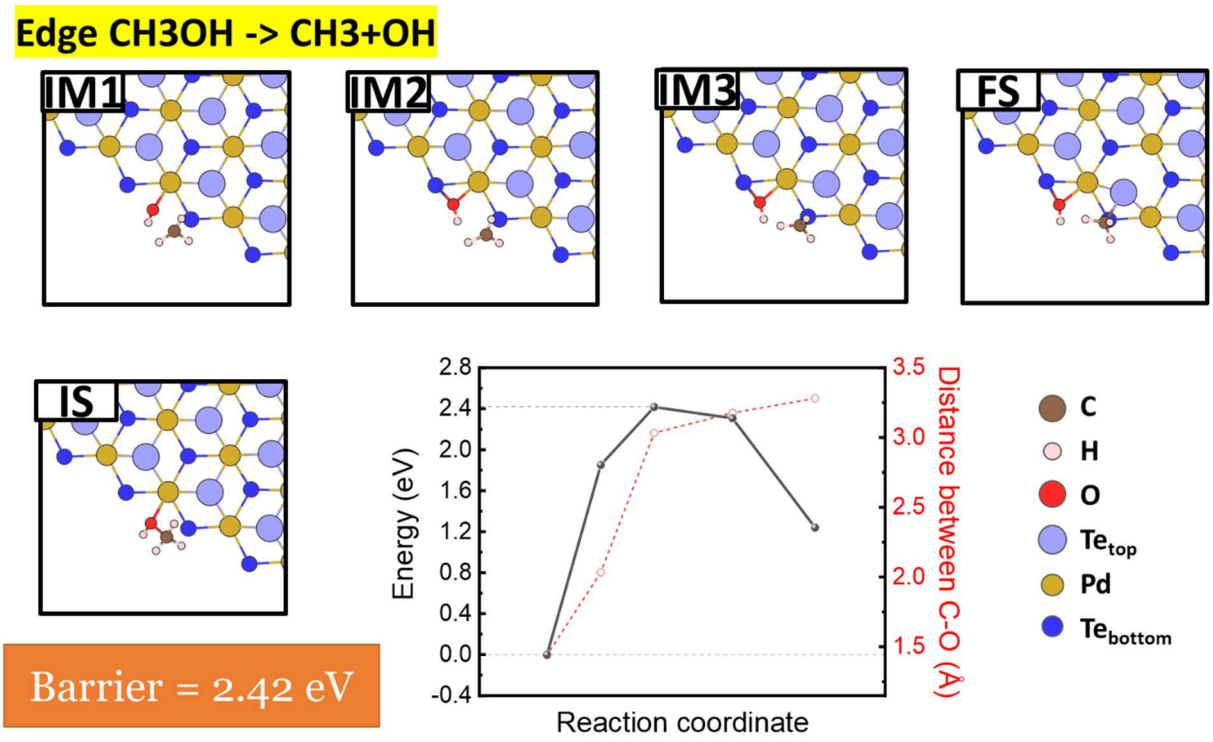


**Figure 27.** The energy profile of C-O bond scission of $CH_3OH$ on the edge sites of a $PdTe_2$ island. The energy barrier is 2.42 eV. Details of initial state (IS), CINEB images (IM) and final state (FS) are presented. The red dashed line indicates the variation of the C-O distance.

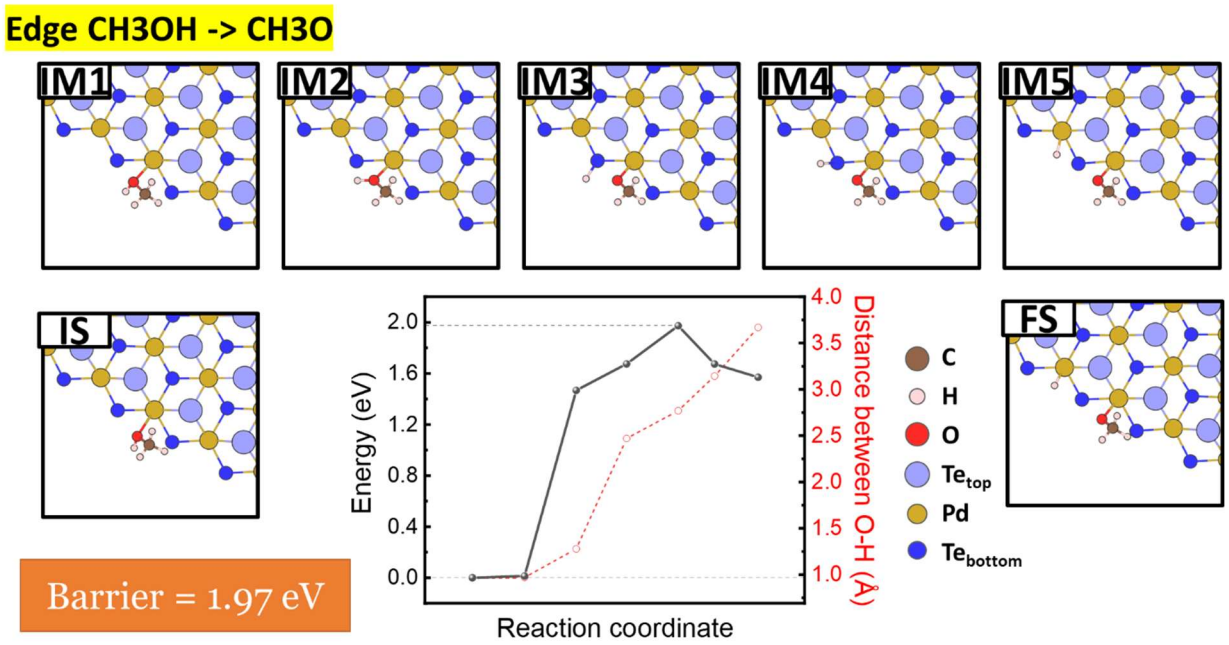


**Figure 28.** The energy profile of dehydrogenation of methanol ($CH_3OH$) to methoxy ($CH_3O$) on the edge sites of a $PdTe_2$ island. The energy barrier is 1.97 eV. Details of initial state (IS), CINEB images (IM) and final state (FS) are presented. The red dashed line indicates the variation of the O-H distance.

**Supplementary References**

1. J. Li, T. Joseph, M. Ghorbani-Asl, S. Kolekar, A.V. Krasheninnikov, M. Batzill, Advanced Functional Materials **32**, 2110428 (2022).